Crystal structure and ferromagnetism of the $CeFe_9Si_4$ intermetallic compound

Primož Koželj,[1,2] Stanislav Vrtnik,[1] Justine Boutbien,[3] Jože Luzar,[1] Andreja Jelen,[1] Sorour Semsari Parapari,[1] Pascal Boulet,[3,§] Marie-Cécile de Weerd,[3] Gwladys Lengaigne,[3] Magdalena Wencka,[1,4] Vincent Fournée,[3] Julian Ledieu,[3] Sašo Šturm,[1] Janez Dolinšek[1,2,*]

[1] *J. Stefan Institute, Jamova 39, SI-1000 Ljubljana, Slovenia*

[2] *University of Ljubljana, Faculty of Mathematics and Physics, Jadranska 19, SI-1000 Ljubljana, Slovenia*

[3] *Institut Jean Lamour, UMR 7198 CNRS – Université de Lorraine, Campus Artem, 2 allée André Guinier, BP 50840, F-54011 Nancy, France*

[4] *Institute of Molecular Physics, Polish Academy of Sciences, Smoluchowskiego 17, PL-60-179 Poznań, Poland*

[§] Corresponding author. *E-mail address*: p.boulet@univ-lorraine.fr (P. Boulet).

* Corresponding author. *E-mail address*: janez.dolinsek@ijs.si (J. Dolinšek).

Abstract

We have determined the crystal structure and the magnetic state of the $CeFe_9Si_4$ intermetallic compound. Our revised structural model (fully ordered tetragonal unit cell, *I*4/*mcm*) agrees with the previous literature report, except for some minor quantitative differences. Magnetically, the $CeFe_9Si_4$ undergoes a ferromagnetic transition at the temperature $T_C \approx 94$ K. Ferromagnetism in the combined Ce–Fe spin system is a result of interplay between the localized magnetism of the Ce sublattice and the Fe band (itinerant) magnetism. Ferromagnetic ordering obeys the rather general rule that the exchange spin coupling between atoms possessing more than half full *d* shells with atoms possessing less than half full *d* shells is antiferromagnetic (where the Ce atoms are considered as light *d* elements). Since in rare-earth metals from the light half of the lanthanide series, the magnetic moment is directed opposite to the spin, this results in ferromagnetism. The magnetoresistance and the magnetic specific heat show additional temperature-dependent feature (a shoulder) deep inside the ferromagnetic phase that is considered to originate from the influence of the magnetization on the electronic band structure via the magnetoelastic coupling, which alters the Fe band magnetism below T_C. The ferromagnetic phase of $CeFe_9Si_4$ is magnetically soft.

1. INTRODUCTION

Many cerium (Ce)-containing intermetallic compounds show uncommon magnetic and electronic transport properties, originating from the fact that the spatial extent of the Ce 4*f* wave function (containing one electron in the 4*f* shell) is the largest among the lanthanide series, which makes the exchange interaction between the localized 4*f* electron and the conduction electrons especially strong. The properties include highly localized magnetism, often with very anisotropic interactions, mixed-valence phenomena, single-ion Kondo effect and Kondo lattice with strongly quenched magnetic moments, heavy-fermion behavior, unconventional superconductivity and quantum criticality. The Ce compounds and their properties have been reviewed by Sereni.[1] Interesting Kondo-lattice behavior was reported for the $CeNi_9Si_4$ compound,[2] which crystallizes in a fully ordered tetragonal (*I*4/*mcm*) variant of the $NaZn_{13}$-type cubic structure. In the $CeNi_9Si_4$, Ni ions do not carry magnetic moments, so that the magnetism and the Kondo lattice originate from the Ce sublattice (the La-substituted counterpart $LaNi_9Si_4$ is nonmagnetic[2]). The low-temperature Kondo lattice in the $CeNi_9Si_4$ is considered to be exceptional among the Kondo-lattice systems due to the low Ce fraction of 7 at.% that makes the nearest-neighbor Ce–Ce distances large (5.6 Å) and the Ce–Ce intersite interactions weak. In our research, we have synthesized the $CeFe_9Si_4$ compound, by replacing Ni (that is nonmagnetic in the $CeNi_9Si_4$) with another magnetic transition element Fe. We have characterized the magnetic state of the combined system of localized Ce moments, interacting with the band magnetism of the itinerant Fe moments, by performing measurements of the magnetization, magnetoresistance and magnetic specific heat. For the $CeFe_9Si_4$ phase, there is already one crystallographic structure report in literature, obtained in a study of the isothermal section at 900 ^{o}C of the Ce–Fe–Si ternary system.[3] We have re-

determined the crystal structure, complemented it with additional information and compared it with the existing report.[3]

2. MATERIAL SYNTHESIS AND CHARACTERIZATION

The elements Ce of grade 3N, Fe (2N5) and Si (2N5) were alloyed in an arc-melting furnace under 700 mbar Ar atmosphere. The as-cast button was wrapped in a tantalum foil and then annealed in a quartz tube with Ar + 5% H_2 atmosphere for 10 days@900 ^{o}C, followed by 5 days@1140 ^{o}C. The final material was polygrain with the grains' cross dimensions of several 10 µm.

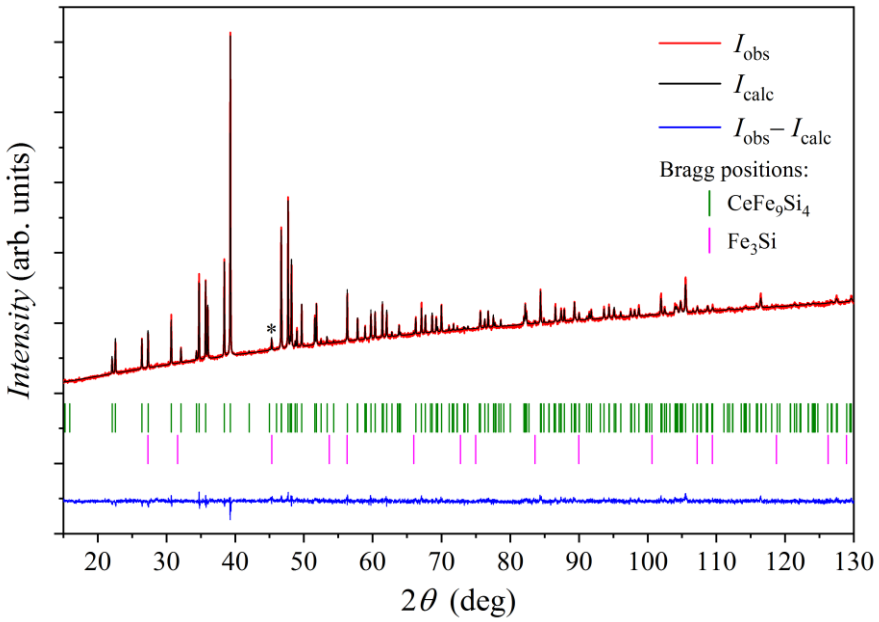

Fig. 1. XRD pattern of the $CeFe_9Si_4$ polygrain material with the Rietveld refinement. The upper two traces (overlaid) represent the observed intensity I_{obs} (red) and the calculated intensity I_{calc} (black), whereas the difference $I_{obs} - I_{calc}$ is shown in the bottom-most trace (blue). Bragg positions of the $CeFe_9Si_4$ and Fe_3Si phases are shown as stick spectra. The

most intense diffraction peak of the Fe_3Si impurity phase (at $2\theta = 45.24^o$) is marked by an asterisk.

X-ray diffraction (XRD) powder pattern using Cu Kα_1 X-ray source is shown in Fig. 1 (the XRD experimental details are given in the Experimental section). The diffraction pattern reveals a tetragonal structure, space group *I*4/*mcm*, unit cell parameters $a = 7.8929(1)$ Å and $c = 11.6653(2)$ Å. To check the purity of the investigated $CeFe_9Si_4$ material, we performed Rietveld refinement using Fullprof software.[4] The result is shown in Fig. 1. The Fe_3Si impurity phase was detected (body-centered cubic, $Fm\bar{3}m$, $a = 5.6644(3)$ Å)[5,6] in the amount of 5.7(3) wt.%. The most clearly observed diffraction peak of the Fe_3Si phase is the one at $2\theta = 45.24^o$ (marked by an asterisk), while the other peaks are either hidden behind the peaks of the main $CeFe_9Si_4$ phase or are too weak.

A scanning electron microscopy backscattered electron (SEM-BSE) image of the material is shown in Fig. 2. The medium-gray matrix contains darker-gray precipitates of several 10-μm cross dimensions and some additional white "spots". Some porosity, estimated at 0.5% volume fraction, is also visible in the material. The compositions of the three phases were checked by energy-dispersive X-ray spectroscopy (EDS). The composition of the matrix (in at.%, rounded to the nearest integers) is $Ce_7Fe_{63}Si_{30}$, corresponding almost exactly to the stoichiometric formula $CeFe_9Si_4$. The composition of the darker-gray precipitates is $Fe_{77}Si_{23}$, corresponding to the phase stoichiometry Fe_3Si, while the composition of the white spots is $Ce_{20}Fe_{41}Si_{39}$, corresponding to $CeFe_2Si_2$. The $CeFe_2Si_2$ phase (tetragonal, *I*4/*mmm*)[7,8] is another impurity in the investigated $CeFe_9Si_4$ material, but its amount is very low, estimated at 0.5 wt.%.

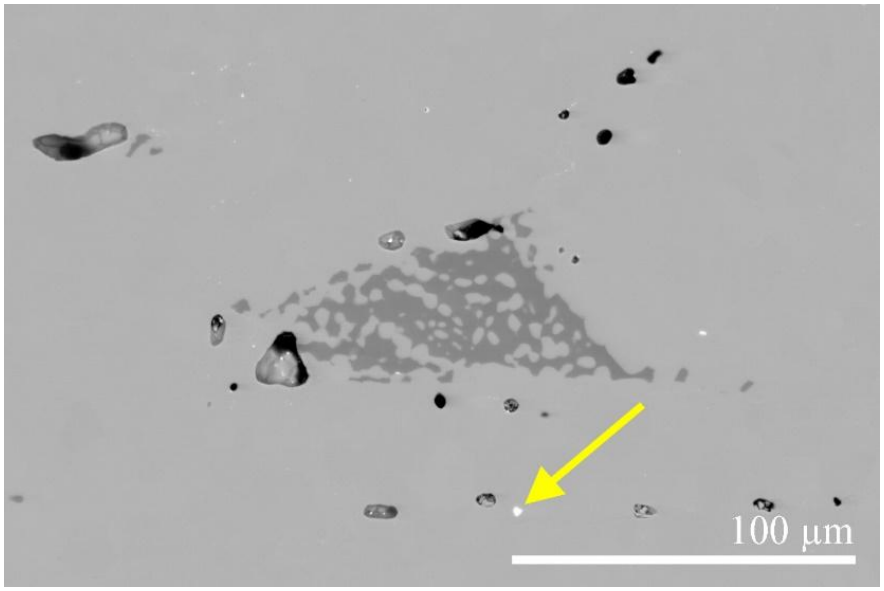

Fig. 2. SEM-BSE image of the $CeFe_9Si_4$ material. The matrix is the $CeFe_9Si_4$ phase, the darker-grey precipitates are the Fe_3Si phase and the white "spots" (one marked by an arrow) are the $CeFe_2Si_2$ phase. Some porosity is also visible.

High-angle annular dark-field scanning transmission electron microscopy (HAADF-STEM) experiments were performed to investigate potential planar defects, such as misfits, dislocations, inversion boundaries, etc., at the atomic scale. HAADF-STEM images of the $CeFe_9Si_4$ structure are shown in Fig. 3 (experimental details are described in the Experimental section). In Fig. 3a, a representative low-magnification image (often referred to as the *Z*-contrast image), viewed along the [111] crystallographic direction is shown. The analysis of the corresponding experimental selected-area electron diffraction (SAED) pattern in the [111] zone axis (superimposed in Fig. 3a) is in agreement with the predicted crystal structure. No planar defects could be detected in the observed specimen region. A representative high-magnification experimental atomic-resolution HAADF-STEM image, viewed along the [111] direction, is shown in Fig. 3b. The contrast variation in the atomic-resolution *Z*-contrast images is roughly following a Z^2 dependence on the average atomic number of the probed

atom column, which makes the reconstruction of both the atom types and the atomic arrangements of the underlying crystal lattice straightforward. In this regard, the highest-contrast regions in Fig. 3b are associated with the fully occupied Ce atomic columns (Z = 58), followed by Fe (Z = 26) and Si (Z = 14) atomic columns, respectively, visualized as lower-intensity regions. The Ce atomic columns are clearly visible in the experimental HAADF-STEM image, while the singular Fe and Si atomic columns cannot be resolved since the small projected distances between the neighboring Fe and Si columns are beyond the given spatial resolution of the electron probe. The constructed $CeFe_9Si_4$ atomic model (as determined by single-crystal XRD, presented in the continuation) viewed along the [111] direction is superimposed on the HAADF-STEM atomically resolved image, and fits well with the underlying experimental structure.

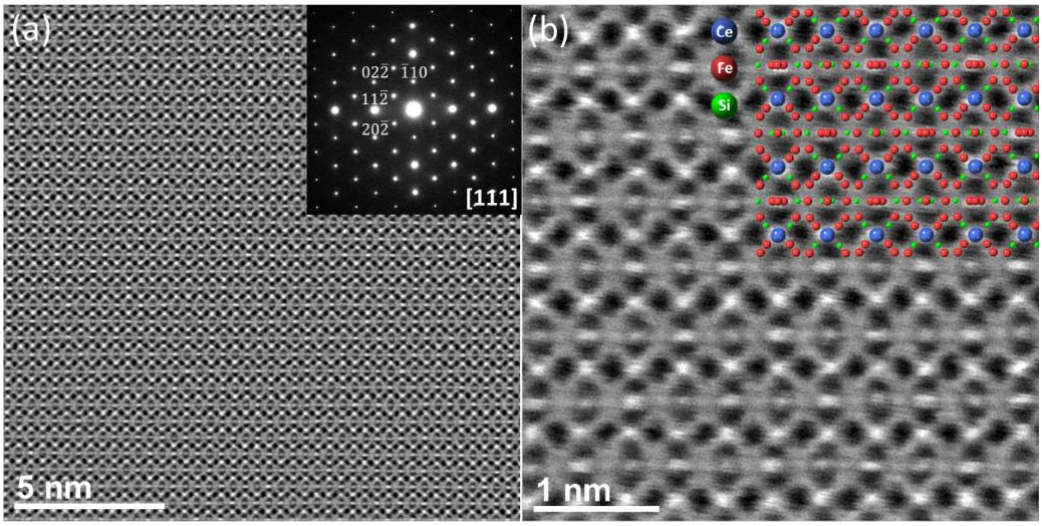

Fig. 3. (a) Atomically-resolved experimental unprocessed HAADF-STEM image of the $CeFe_9Si_4$ crystal, with a superimposed SAED pattern in the [111] zone axis. **(b)** High-resolution ABSF-filtered HAADF-STEM image viewed along the [111] crystallographic direction, together with the superimposed atomic model. Blue, red, and green balls represent Ce, Fe, and Si atoms, respectively.

3. STRUCTURAL MODEL

The structure was determined by single-crystal XRD using a molybdenum Kα X-ray source. A $CeFe_9Si_4$ specimen of approximate dimensions 50×40×30 μm^3 was used for the crystallographic analysis. The total exposure time was 18.18 hours. The frames were integrated with the Bruker SAINT software package using a narrow-frame algorithm. The integration of the data using a tetragonal unit cell yielded a total of 8006 reflections to a maximum θ angle of 24.908°, of which 191 were independent (average redundancy 41.916, completeness 100.0%) and 186 (97.38%) were greater than $2\sigma(F^2)$. The crystal structure was solved in the centrosymmetric space group *I*4/*mcm* (No. 140), with the final cell constants a = 7.8912(11) Å and c = 11.6535(16) Å based upon the refinement of the XYZ-centroids of 7021 reflections above 20 $\sigma(I)$ with 6.993° < 2θ < 59.79°. Data were corrected for the absorption effects using the multi-scan method (SADABS). The ratio of minimum to maximum apparent transmission was 0.751. The calculated minimum and maximum transmission coefficients (based on the crystal size) were 0.379 and 0.532. All atomic positions were obtained by direct methods (SIR2014) and were in agreement with the positions assigned during the Ce–Fe–Si ternary phase diagram investigations by powder XRD,[3] showing in particular that all sites are fully occupied without any Fe,Si mixed occupancy. The final reliability factors including the anisotropic thermal factor converged at $R1$ = 0.0062, $wR2$ = 0.0152 with $I > 2\sigma(I)$ and $R1$ = 0.0065, $wR2$ = 0.0153 with all reflections. The goodness-of-fit (GOF) was 1.13. The largest peak in the final difference electron density synthesis was 0.25 $e^-Å^{-3}$ and the largest hole was –0.21 $e^-Å^{-3}$ with an RMS deviation of 0.062 $e^-Å^{-3}$. On the basis of the final model, the calculated density was 6.912 g cm^{-3} and F(000) 1392 e^-. The above figures did not change when refining the occupancy

factors of the atomic sites. This result confirms that the composition of our crystal is in good agreement with the starting composition $CeFe_9Si_4$. The X-ray crystallographic data are summarized in Table 1 (also presented in the supplementary CIF file, deposited in the Cambridge Structural Database as the number CSD 2217058).

Table 1. X-ray crystallographic data for $CeFe_9Si_4$ (CSD deposition number 2217058).

Chemical formula	$CeFe_9Si_4$	
Formula weight (g mol^{-1})	755.13	
Temperature (K)	296(2)	
Wavelength (Å)	0.71073 for single-crystal data 1.5406 for powder data	
Crystal size (μm^3)	50×40×30	
Crystal system	tetragonal	
Space group	*I*4/*mcm* (No. 140)	
Unit cell dimensions (Å)	single crystal	powder
	$a = 7.8912(11)$	$a = 7.8929(1)$
	$c = 11.6535(16)$	$c = 11.6653(2)$
Volume ($Å^3$)	725.7(2)	726.73(1)
Z	4	
Calculated density (g cm^{-3})	6.912	
Absorption coefficient (mm^{-1})	24.11	
F(000)	1392	
θ range for data collection (deg)	3.497–24.908	
Index ranges	$-8 \leq h, k \leq 8,\ -12 \leq l \leq 12$	
Collected, indep reflns	8006/191	
Coverage of the reciprocal sphere (%)	100	
GOF	1.13	
R indices ($I > 2\sigma(I)$)	*R*(int) = 0.035, *R*1 = 0.0062, *wR*2 = 0.0152	

All Powder refinement	R(int) = 0.035, R1 = 0.0065, wR2 = 0.0153 R_B = 0.106, R_f = 0.127
Extinction coeff	0.00042(7)
Number of parameters refined	25
$\Delta\rho_{max}$, $\Delta\rho_{min}$ (e^{-}Å^{-3})	0.25/–0.21

Table 2. Atomic coordinates and isotropic displacement parameters for $CeFe_9Si_4$ from the single crystal refinement. The values obtained from the powder X-ray refinement are given in the second line for the Fe1, Fe2 and Si crystallographic sites.

Atom name	Site	x	y	z	U_{eq} (Å^2)	occupancy
Ce	4*a*	0.0	0.0	1/4	0.00585(11)	1
Fe1	16*l*	0.37742(3) 0.3776(1)	0.12258(3) 0.1223(2)	0.32124(3) 0.3218(2)	0.00524(13)	1
Fe2	16*k*	0.06618(4) 0.0663(3)	0.20002(4) 0.2007(3)	0.0 0.0	0.00579(13)	1
Fe3	4*d*	1/2	0.0	1/2	0.00486(16)	1
Si	16*l*	0.32671(6) 0.3247(4)	0.17329(6) 0.1752(4)	0.12219(6) 0.1212(4)	0.00612(17)	1

Table 3. Anisotropic atomic displacement parameters (Å^2) for $CeFe_9Si_4$.

	U_{11}	U_{22}	U_{33}	U_{23}	U_{13}	U_{12}
Ce	0.00604(13)	0.00604(13)	0.00549(16)	0	0	0
Fe1	0.00596(16)	0.00596(16)	0.0038(2)	0.00043(9)	–0.00043(9)	–0.00014(14)
Fe2	0.0055(2)	0.0068(2)	0.0050(2)	0	0	–0.00080(14)
Fe3	0.0055(2)	0.0055(2)	0.0035(3)	0	0	–0.0002(3)

Si	0.0067(2)	0.0067(2)	0.0049(3)	–0.00003(18)	0.00003(18)	0.0012(3)

Solving the structure has generated five independent crystallographic sites in the tetragonal unit cell (Table 2). All sites are fully ordered (occupation 1, no mixed-populated sites), labeled as Ce (Wyckoff position 4*a*), Fe1 (16*l*), Fe2 (16*k*), Fe3 (4*d*) and Si (16*l*). The unit cell contains 56 atoms. The isotropic atomic displacement parameters U_{eq} of all sites (also given in Table 2) are quite similar. The anisotropic atomic displacement parameters are presented in Table 3.

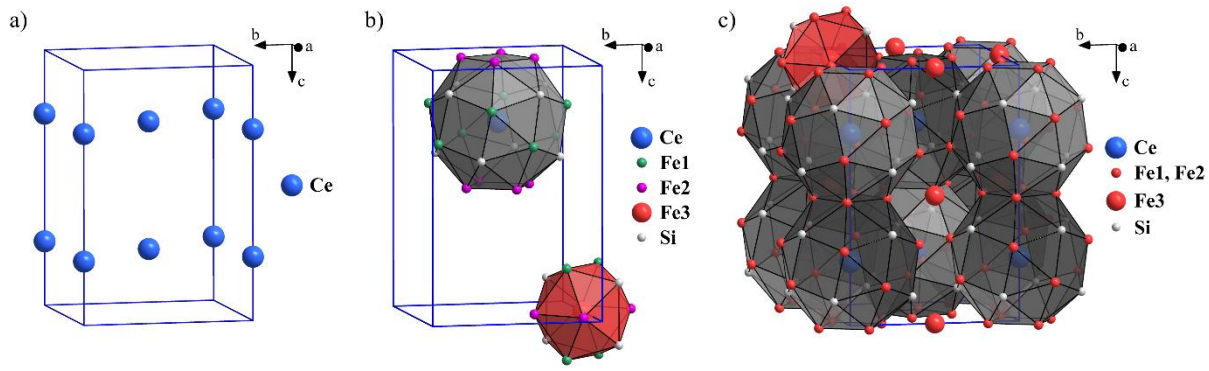

Fig. 4. The $CeFe_9Si_4$ tetragonal unit cell. **(a)** The cerium sublattice; **(b)** One 24-atom polyhedron (the "cage") around the central Ce atom and one icosahedron around the central Fe1 atom; **(c)** The complete unit cell.

The structure description begins by first considering the Ce sublattice, which is shown in Fig. 4a. Adding the Fe and Si atoms, it is apparent that each Ce atom is located in the center of a "cage", a polyhedron composed of 24 atoms (eight Fe1, eight Fe2 and eight Si), distributed on 32 triangles, four rectangles and two squares. One such cage is depicted in Fig. 4b. The triangles are not equilateral and the two squares (having a tiny rhombic distortion) are formed from the Fe2 atoms. The radial distances between the central Ce atom and the cage atoms are Ce–Fe1 3.2396 Å, Ce–Fe2 3.3544 Å and Ce–Si 3.2765 Å. The only remaining

atoms, which are not incorporated into the cages, are the Fe3 atoms. Each of these is icosahedrally coordinated by four Fe1, four Fe2 and four Si atoms that all already belong to the 24-atom cages. The Fe3 atoms are located in the centers of the icosahedra and the radial distances to the atoms on the icosahedra are Fe3–Fe1 2.4922 Å, Fe3–Fe2 2.4242 Å and Fe3–Si 2.4016 Å. One such icosahedron is shown in Fig. 4b. Note that in Fig. 4b, the Fe1, Fe2 and Fe3 atoms are distinguished by different colors and Fe3 is drawn in larger size. The tetragonal unit cell is depicted in Fig. 4c (there, the Fe1, Fe2 and Fe3 atoms are all presented in the same color, but Fe3 has larger size). The distribution of cages in the unit cell follows the distribution of the Ce atoms. One Fe3-centered icosahedron in also drawn. The type of structure presented in Fig. 4 is not unique to the $CeFe_9Si_4$, but was found before in the ACu_9X_4 (A = Sr, Ba; X = Si, Ge) series,[9] $LaFe_9Si_4$,[10] $CeNi_9Si_4$,[2] and in the Sn-for-Si substituted rare-earth (RE)-containing compounds $RECu_9Sn_4$ with RE = La to Nd,[11,12] Eu[13,12] and Yb.[14] Comparing the tetragonal unit cell parameters of the $CeFe_9Si_4$ from this work (a = 7.8912(11) Å, c = 11.6535(16) Å from single-crystal XRD and a = 7.8929(1) Å, c = 11.6653(2) Å from powder XRD) to the previous report on the same compound[3] (a = 7.892(1) Å, c = 11.666(1) Å), the differences are minute. The anisotropic displacement parameters in Table 3 are, however, additionally presented (not included in the crystallographic information in[3]).

4. PHYSICAL PROPERTIES

4.1. Magnetization versus temperature. The direct-current (dc) magnetization of the $CeFe_9Si_4$ sample was first determined in the temperature range 10–400 K using a SQUID magnetometer (experimental details are described in the Experimental section). The zero-

field-cooled (zfc) and field-cooled (fc) magnetization curves in a magnetic field $\mu_0 H = 0.1$ T, as a function of temperature, are presented in Fig. 5a. A ferromagnetic (FM) transition is observed at $T_C \approx 94$ K and the two curves overlap perfectly down to the lowest temperature (i.e., there is no splitting between M_{zfc} and M_{fc}). The small positive, constant-like offset of the baseline above T_C (of magnitude about 1.2 $\mathrm{Am^2kg^{-1}}$, in mass magnetization units) that persists up to 400 K indicates that this signal could originate from another FM fraction in the sample.

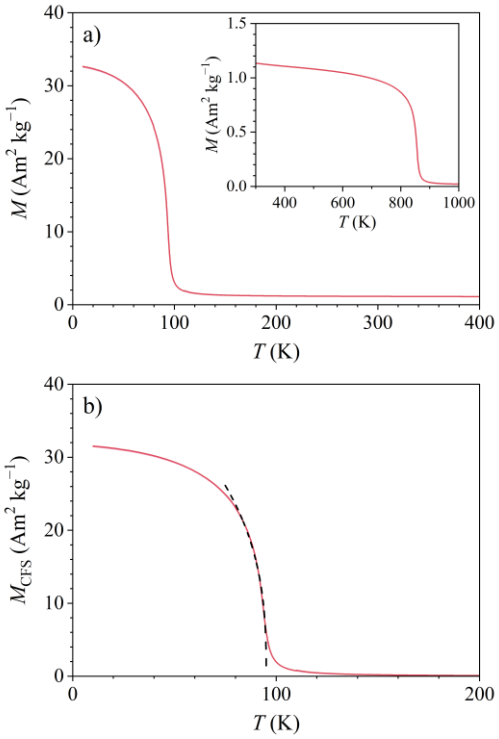

Fig. 5. (a) Zfc and fc magnetization curves of the $CeFe_9Si_4$ sample in a magnetic field $\mu_0 H = 0.1$ T in the temperature range 10–400 K (M_{zfc} and M_{fc} are indistinguishable on the graph). The inset shows M_{zfc} in the temperature range 300–1000 K. **(b)** The magnetization of the $CeFe_9Si_4$ phase only (M_{CFS}), obtained by subtracting the magnetization of the Fe_3Si impurity phase M_{FS} from the total signal below 300 K. Dashed curve is the fit within the critical region with the formula $M_{CFS} \propto (T_C - T)^{\beta}$ (see text).

To find out the origin of this "high-temperature" FM signal, we have repeated the $M(T)$ measurement in the same field, this time using a furnace operating between 300 and 1000 K. The $M(T)$ curve is shown in the inset of Fig. 5a, where an FM transition at about 840 K is evident. This transition temperature is the same as the FM transition temperature reported in literature for the Fe_3Si compound.[5] Since the Fe_3Si is present as an impurity phase in the investigated $CeFe_9Si_4$ material (in the amount of 5.7 wt.%), it is straightforward to assign the high-temperature FM signal to the Fe_3Si inclusions (the second impurity phase, $CeFe_2Si_2$ at 0.5 wt.%, is a Pauli paramagnet[7,8] and contributes negligibly to the total signal). At 300 K, the magnitude of the Fe_3Si signal amounts to $M_{FS} = 1.13$ Am^2kg^{-1}, accounting well for the baseline offset above T_C in the main panel of Fig. 5a. The total magnetization of the sample ($CeFe_9Si_4$ phase plus Fe_3Si inclusions) at 10 K in a 0.1 T field amounts to $M_{CFS} + M_{FS} = 33$ Am^2kg^{-1} and since the M_{FS} signal is practically constant below room temperature, it constitutes about 3% of the total magnetization at 10 K. For the analysis of the $CeFe_9Si_4$ FM phase, we have subtracted the constant offset (M_{FS}) from the total signal in the low-temperature range below 300 K, and the resulting $CeFe_9Si_4$-only magnetization M_{CFS} is shown in Fig. 5b. The magnetization within the critical temperature region just below T_C was fitted with the formula $M_{CFS} \propto (T_C - T)^{\beta}$ (dashed curve in Fig. 5b), yielding the critical exponent $\beta = 0.36$.

4.2. Magnetization versus magnetic field. The magnetization versus the magnetic field, $M(H)$, curves of the $CeFe_9Si_4$ sample were measured in the field range ± 7 T. The $M(H)$ curves at temperatures between 400 and 10 K are shown in Fig. 6a. Two types of the $M(H)$ curves are evident, corresponding to the temperature regions above and below $T_C \approx 94$ K.

Below 94 K, the curves are typical ferromagnetic, with a very rapid increase in the low-field region around $H = 0$ and practically no hysteresis (to be discussed later), indicating a magnetically soft material. The saturation magnetization at $T = 10$ K in a 7-T field amounts to $M^{sat} = 46$ Am^{2}kg^{-1}. We keep in mind that this is the total saturation magnetization of the $CeFe_9Si_4$ phase plus the Fe_3Si inclusions. Above 94 K, the $CeFe_9Si_4$ matrix is in the paramagnetic phase, while the Fe_3Si inclusions are in the FM phase. This is mirrored in the shape of the $M(H)$ curves, which are at temperatures considerably higher than 94 K (i.e. at 200, 300 and 400 K in Fig. 6a) a sum of a term linear in H, corresponding to the paramagnetic magnetization of the $CeFe_9Si_4$ phase and an FM term due to the Fe_3Si inclusions. The field-dependence of the $CeFe_9Si_4$ paramagnetic magnetization is in fact given by the Brillouin function, which reduces to a linear-in-H dependence at high temperatures.

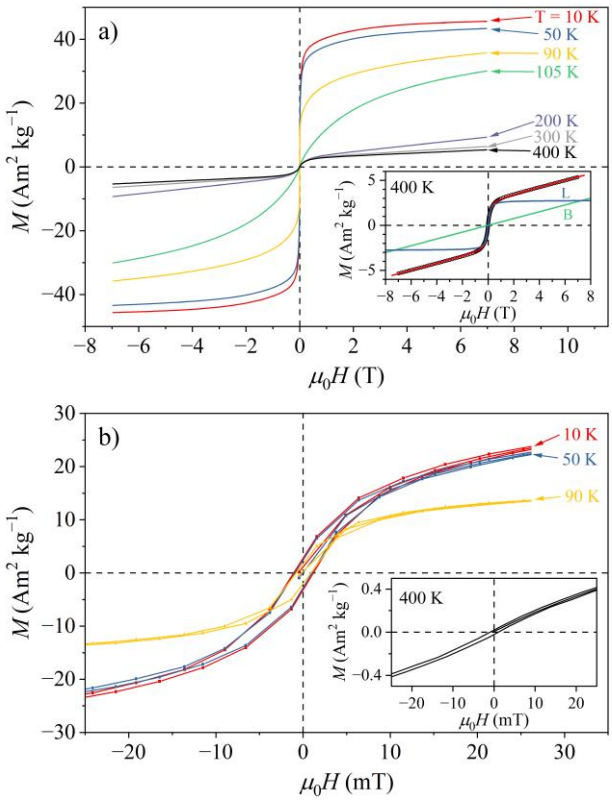

Fig. 6. (a) $M(H)$ curves of the $CeFe_9Si_4$ sample at temperatures between 400 and 10 K. The inset shows the $M(H)$ curve at 400 K on an expanded vertical scale, together with the fit

$M = M_{CFS} + M_{FS}$ (red curve) described in the text (M_{CFS} is the magnetization of the $CeFe_9Si_4$ phase and M_{FS} the magnetization of the Fe_3Si impurity phase). The M_{CFS} paramagnetic contribution to the total fit marked with B (standing for "Brillouin") and the M_{FS} FM contribution marked with L (standing for "Langevin") are also shown. **(b)** The $M(H)$ curves at temperatures 10, 50, 90 and 400 K on an expanded scale about the origin, to show the hysteresis.

The $T = 400$ K $M(H)$ curve is shown on an expanded scale in the inset of Fig. 6a, together with the fit $M = M_{CFS} + M_{FS} = k\mu_0 H + M_{FS}^{sat}\mathcal{L}(x)$. Here $k\mu_0$ is the paramagnetic susceptibility of the $CeFe_9Si_4$ phase, M_{FS}^{sat} is the saturation magnetization of the Fe_3Si inclusions and $\mathcal{L}(x) = \coth x - 1/x$ is the Langevin function, with $x = \mu_0\mu H/k_B T$. Within the Langevin model (which is suitable to reproduce the FM-type $M(H)$ curves, but not their hysteresis), the magnetic moment μ is a classical vector that can assume any value ($\mu \to \infty$), accounting for the large group magnetic moment of the FM phase. The fit-determined parameters are $k = 0.38$ $Am^2kg^{-1}T^{-1}$, $M_{FS}^{sat} = 2.8$ Am^2kg^{-1} and $\mu = 7319\mu_B$, where μ_B is the Bohr magneton. Knowing M_{FS}^{sat} at 400 K (and assuming that this value does not change much down to 10 K), we are able to estimate the saturation magnetization of the $CeFe_9Si_4$ phase as $M_{CFS}^{sat} = M^{sat} - M_{FS}^{sat} \approx 43$ Am^2kg^{-1}. Recalculating this value in units of μ_B per formula unit (f.u.), i.e., per one $CeFe_9Si_4$ "molecule", we obtain $M_{CFS}^{sat} = 5.7$ μ_B/f.u., accounting for the total magnetic moment of one Ce ion and nine Fe. The above value can be contrasted to the estimated maximum possible magnetic moment of one formula unit ($\mu_{f.u.}$), by taking literature values of the saturation moment of a Ce^{3+} ion $\mu_{Ce} = 2.14\mu_B$[15] and ionic values of the iron moments ($\mu_{Fe^{3+}} = 5.9\mu_B$, $\mu_{Fe^{2+}} = 5.4\mu_B$)[16], yielding $\mu_{f.u.}$ in the range 50–55 μ_B. Using the ionic values of the iron moments implicitly assumes that they are localized (like in

an insulator), so that the much smaller experimental value of 5.7 μ_B is a strong indication of itinerant (band) magnetism of the Fe subsystem in the $CeFe_9Si_4$. The moments of the Ce sublattice are, however, localized.

Searching for the magnetization hysteresis, palladium correction was applied to the $M(H)$ curves to remove the small hysteresis of the superconducting magnet of the employed SQUID magnetometer. The $M(H)$ curves at the temperatures 10, 50, 90 and 400 K are presented in Fig. 6b on an expanded scale about the origin. A tiny hysteresis with the same coercive field of $\mu_0 H_c = 1.0 \pm 0.1$ mT is observed at all temperatures, also at 400 K that is high above the FM transition in the $CeFe_9Si_4$. This indicates that the hysteresis originates from the Fe_3Si impurity phase and confirms the practically ideal magnetic softness of the $CeFe_9Si_4$ FM phase.

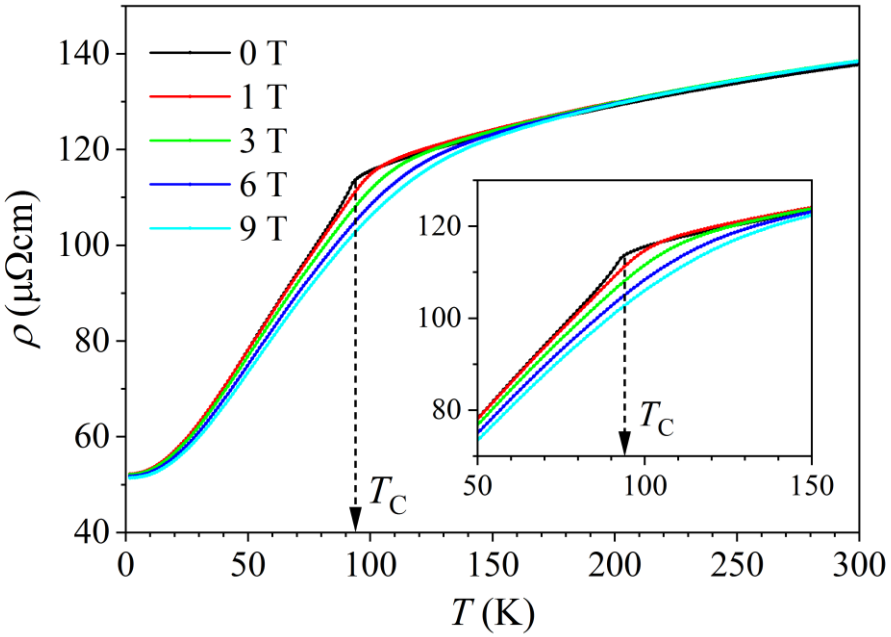

Fig. 7. Electrical resistivity of the $CeFe_9Si_4$ sample at temperatures between 2 and 300 K in selected magnetic fields in the range $\mu_0 H =$ 0–9 T (values indicated on the graph). Expanded portions of the resistivity curves around T_C are shown in the inset.

4.3. Electrical resistivity and magnetoresistance. The electrical resistivity of the $CeFe_9Si_4$ sample at temperatures between 2 and 300 K in the magnetic field range $\mu_0 H =$ 0–9 T is shown in Fig. 7. The resistivity $\rho(H,T)$ increases with temperature and is field-independent in the limits much below and much above the FM transition temperature $T_C \approx 94$ K, while it is strongly field-dependent in the region of T_C. The 2-K residual resistivity amounts to $\rho_{2K} =$ 52 μΩcm, while the room-temperature resistivity is $\rho_{300K} = 137$ μΩcm. In zero magnetic field, the resistivity shows a discontinuous change of slope at T_C, where the slope is larger below T_C and smaller above. In an increasing magnetic field, the discontinuous change of slope at T_C becomes rounded and smeared and the resistivity continuously decreases within the T_C region. Such temperature- and field-dependence of the resistivity is typical of a conducting ferromagnet. According to the Matthiessen's rule, the resistivity is a sum of a temperature-independent term ρ_0 due to the elastic scattering of conduction electrons by quenched impurities (this term determines the low-temperature residual resistivity), the temperature-dependent term due to phonon scattering ρ_{ph} that increases with temperature as T^n (where $n = 1$ well above the Debye temperature and $n =$ 3–5 far below it) and the FM-specific term ρ_{FM} due to spin-disorder scattering, so that the total resistivity is $\rho = \rho_0 + \rho_{ph} + \rho_{FM}$. The origin of ρ_{FM} is magnetic scattering of conduction electrons by the fluctuating spins that participate in the FM ordering. Upon approaching the T_C, the fluctuating spins create a spin-dependent potential of random character that fluctuates between values differing by the on-site exchange interaction and scatters the conduction electrons. Within the FM phase, the spin-disorder resistivity is given by[17–19]

$$\rho_{FM} = \rho_{para}\{1 - [M(T)/M(0)]^2\}, \quad (1)$$

where M is the spontaneous magnetization of the FM state and ρ_{para} is the resistivity of the paramagnetic state above T_C. ρ_{para} is temperature independent and proportional to the square

of the exchange coupling constant between the localized spins and the conduction electrons. According to Eq. (1), ρ_{FM} is constant above T_C and starts to drop below, giving a discontinuous change of slope in the total ρ at T_C. Applying a magnetic field within the T_C region where the magnetic susceptibility is high, M is increased, thus producing a negative magnetoresistance. All this is consistently observed in the experimental $\rho(H,T)$ curves of Fig. 7. Spin-disorder scattering is pronounced in RE metals and alloys. In the $CeFe_9Si_4$, it is reasonable to consider that it originates mainly from the scattering of conduction electrons by the fluctuating Ce^{3+} moments.

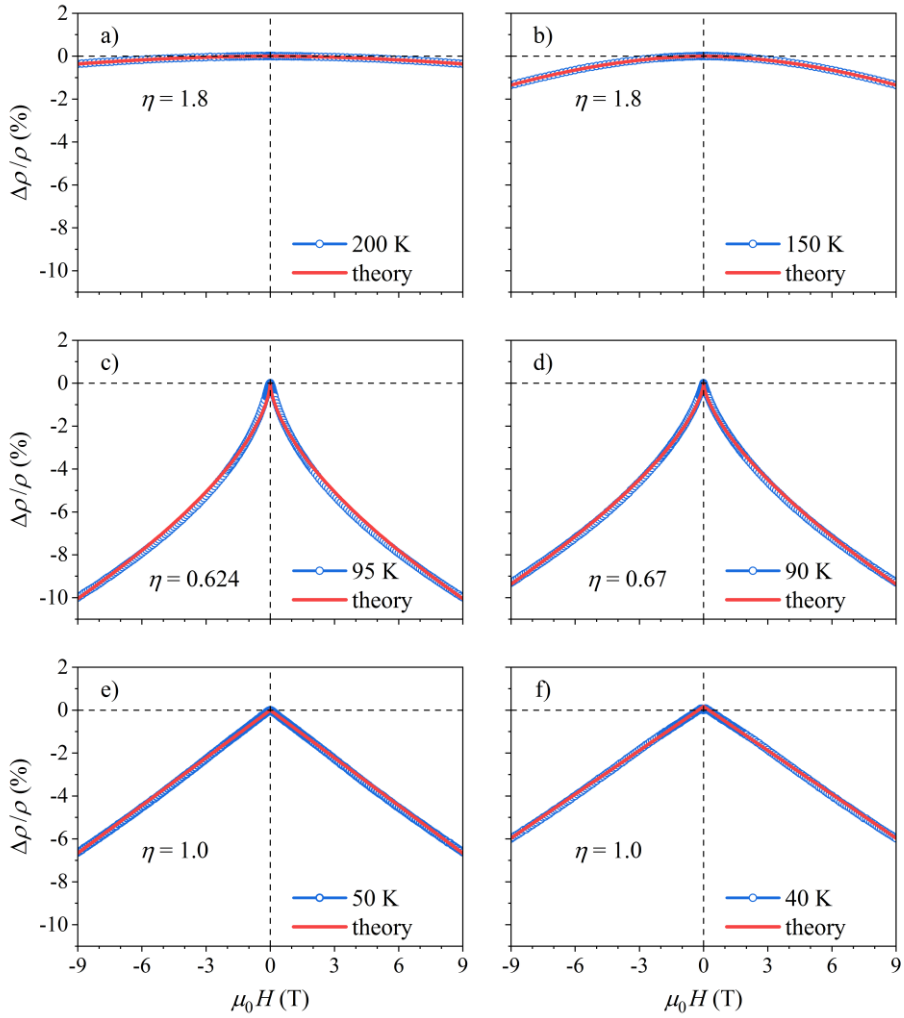

Fig. 8. The magnetoresistance curves, $\Delta\rho/\rho$, of the $CeFe_9Si_4$ sample in the magnetic field range $\mu_0 H = \pm$ 9 T in three characteristic temperature regimes relative to $T_C \approx$ 94 K. The

curves at $T = 200$ K (panel **(a)**) and 150 K (panel **(b)**) belong to the high-temperature regime $T > T_C$; the curves at $T = 95$ K (panel **(c)**) and 90 K (panel **(d)**) are taken in the close vicinity of the FM phase transition (the $T \approx T_C$ regime); the curves at $T = 50$ K (panel **(e)**) and 40 K (panel **(f)**) are taken deep inside the FM phase ($T < T_C$). Solid curves are fits with the mean field theory, described in the text. The values of the power-law fit parameter η are indicated in the graphs.

The magnetoresistance $[\rho(H) - \rho(0)]/\rho(0) = \Delta\rho/\rho$ is another suitable quantity to characterize the magnetic state of a metallic alloy. The magnetoresistance curves of the $CeFe_9Si_4$ sample in the magnetic field range $\mu_0 H = \pm 9$ T in three characteristic temperature regimes relative to $T_C \approx 94$ K are shown in Fig. 8. The $\Delta\rho/\rho$ curves at $T = 200$ K and 150 K (Figs. 8a and 8b) belong to the high-temperature regime $T > T_C$, corresponding to the part of the paramagnetic phase, where short-range ordered spin clusters start to form on approaching the T_C. The curves at $T = 95$ K and 90 K (Figs. 8c and 8d) are taken in the close vicinity of the FM phase transition (the $T \approx T_C$ regime), whereas the curves at $T = 50$ K and 40 K (Figs. 8e and 8f) are taken deep inside the FM phase ($T < T_C$). All $\Delta\rho/\rho$ curves are negative, which is a characteristic feature of the FM-type magnetoresistance, while their magnitude and shape varies according to the temperature regime.

Theoretical expressions for the FM magnetoresistance within the above three characteristic temperature regimes are known in literature. The calculations were first performed in the mean-field theory[20] and then improved by a more involved formalism.[21] Our experimental $\Delta\rho/\rho$ curves presented in Fig. 8 could be well reproduced theoretically already by the simpler mean-field theory, which we discuss in the following. The mean-field predictions are $\Delta\rho/\rho \propto -H^2/(T - T_C)^2$ at $T > T_C$, $\Delta\rho/\rho \propto -H^{2/3}$ at $T \approx T_C$ and $\Delta\rho/\rho \propto -H/\sqrt{T_C - T}$ at $T < T_C$ (the more involved theory[21] brings for the $T \approx T_C$ and $T < T_C$

regimes an extra logarithmic term that multiplies the mean-field result, while the mean-field result for $T > T_C$ remains unchanged). The fits of the experimental magnetoresistance curves in Fig. 8 were all performed with the expression $\Delta\rho/\rho = -\text{const.}\, H^{\eta}$, by treating the power-law exponent η as a free parameter at each measured temperature. The fits of the paraphase magnetoresistance yielded the exponent $\eta = 1.8$ for both measured temperatures of 200 and 150 K (solid curves in Figs. 8a and 8b), which is fairly close to the mean-field value of 2. The small difference could be due to the fact that the mean-field result is valid in the weak-field limit, whereas the experiments were done up to 9 T, which can no more be considered as a weak field. The magnetoresistance very close to T_C was reproduced well with the fit parameter $\eta = 0.62$ at 95 K and $\eta = 0.67$ at 90 K (solid curves in Figs. 8c and 8d), where the second value (0.67) is exactly the mean-field result of 2/3. The magnetoresistance below T_C was reproduced well with the exponent $\eta = 1.0$ (equal to the mean-field result) at both temperatures 50 and 40 K (solid lines in Figs. 8e and 8f). The analysis at still lower temperatures was not done, because the mean-field theory is known to become inadequate in the $T \to 0$ limit.[20]

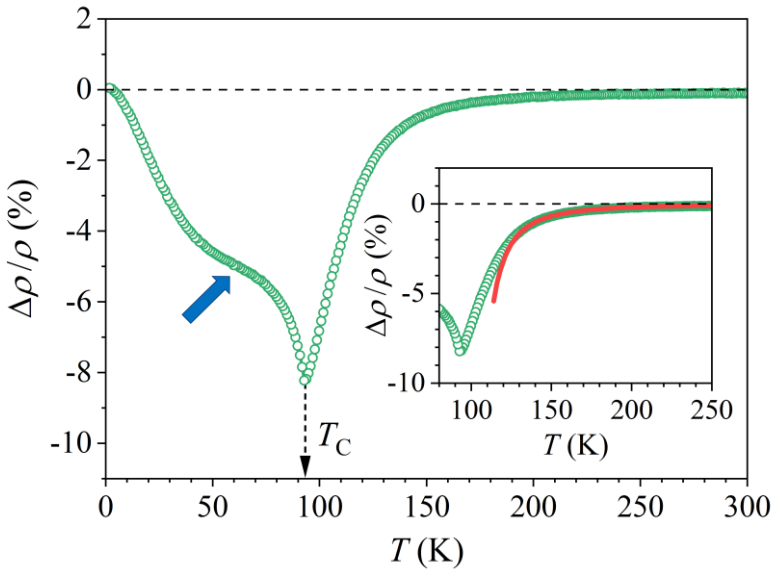

Fig. 9. Magnetoresistance of the $CeFe_9Si_4$ sample in a constant magnetic field $\mu_0 H = 6$ T, measured as a function of temperature in the interval 300–2 K. The shoulder inside the FM phase is marked by an arrow. The inset shows the parabolic fit $\Delta\rho/\rho = -2170\text{K}^2/(T - T_C)^2$ with $T_C = 94$ K (red solid curve) that reproduces well the paramagnetic phase data in the temperature range 250–130 K.

The magnetoresistance as a function of temperature in the interval 300–2 K, measured in a constant magnetic field $\mu_0 H = 6$ T is shown in Fig. 9. Upon cooling from 300 K, the magnetoresistance in the paramagnetic phase becomes nonzero at about 210 K and then decreases (its absolute value $|\Delta\rho/\rho|$ increases) upon approaching the T_C, reaching the minimum in $\Delta\rho/\rho$ (or the maximum in $|\Delta\rho/\rho|$) at $T_C \approx 94$ K. Below T_C, $|\Delta\rho/\rho|$ starts to decrease upon cooling, until it becomes zero in the $T \to 0$ limit. The decrease of $|\Delta\rho/\rho|$ within the FM phase upon cooling is not a simple monotonous one, but a broad shoulder is observed at about 60 K (marked by an arrow in Fig. 9).

The mean-field predictions for the temperature dependence of the magnetoresistance are $\Delta\rho/\rho \propto -1/(T - T_C)^2$ in the paramagnetic phase ($T > T_C$), a minimum in $\Delta\rho/\rho$ at T_C and $\Delta\rho/\rho \propto -1/\sqrt{T_C - T}$ in the FM phase ($T < T_C$). Far away from T_C, the magnetoresistance approaches zero on both sides of the temperature axis (at $T \gg T_C$ and $T \ll T_C$) and the minimum value is reached at T_C, which is all consistently observed in the experimental magnetoresistance of Fig. 9. A parabolic magnetoresistance $\Delta\rho/\rho \propto -1/(T - T_C)^2$ is also observed experimentally in the paramagnetic phase high above T_C, as verified in the inset of Fig. 9, where the parabolic fit reproduces well the experimental data in the temperature range 250–130 K. The experimental magnetoresistance at $T < T_C$ (in the FM phase), however, does not follow the mean-field result $\Delta\rho/\rho \propto -1/\sqrt{T_C - T}$, which predicts a simple monotonous decrease of $|\Delta\rho/\rho|$ upon cooling below T_C, because the

experimental curve exhibits additional shoulder deep inside the FM phase. Theoretically, such shoulder cannot be derived even by the more involved theory of the FM magnetoresistance,[21] so that it is a genuine property of the combined Ce–Fe ferromagnetic spin system in the $CeFe_9Si_4$ crystal. We shall show that the same anomaly (the shoulder) is observed also in the magnetic specific heat.

4.4. Magnetic specific heat. The specific heat C of a conducting ferromagnet is a sum of the electronic (C_{el}), lattice (C_{latt}) and magnetic (C_m) terms, $C = C_{el} + C_{latt} + C_m$. The electronic term $C_{el} = \gamma T$, where γ is the electronic specific heat coefficient, shows linear-in-T dependence up to high temperatures (such as the melting point of the alloy). The lattice contribution is written at low temperatures (typically below 10 K) within the Debye model as $C_{latt} = \alpha T^3$, where the lattice specific heat coefficient α is related to the Debye temperature θ_D via the relation $\theta_D = (12\pi^4 R/5\alpha)^{1/3}$ and R is the gas constant. Since the Debye temperature is usually slightly temperature dependent, this is the low-temperature value of θ_D. The FM contribution at low temperatures can also be written in a simple form, $C_m = \delta T^{3/2}$, representing the contribution due to spin-wave excitations (magnons) of the FM spin system. The total low-temperature specific heat of a ferromagnet is[22]

$$C = \gamma T + \alpha T^3 + \delta T^{3/2}, \qquad (2)$$

which is dominated by the electronic term because of its lowest power T-dependence. The magnetic specific heat C_m vanishes in the $T \to 0$ limit. While the magnon specific heat represents the FM contribution to the total specific heat at low temperatures, there is a much larger magnetic specific heat C_m in the region of the FM phase transition (around T_C), where spin ordering results in a decrease of the magnetic energy that is released from the spin system as heat and detected as an exothermic peak (an anomaly) at T_C in the total specific

heat. We have extracted this magnetic specific heat by a procedure described in the following.

The total specific heat of the $CeFe_9Si_4$ sample in the temperature range 2–300 K, measured in magnetic fields between 0 and 9 T is shown in Fig. 10a in a C vs. T plot. In zero field, a sharp anomaly (a peak) is observed at about 92 K, corresponding to the FM transition temperature T_C (this T_C value is by about 2 K lower than the one determined from the magnetization and magnetoresistance). In an increasing field, the anomaly broadens and smears towards higher temperatures, which is better evident in the inset of Fig. 10a, where the curves are presented on an expanded scale within the phase-transition region. The low-temperature zero-field specific heat in a C/T vs. T^2 plot is shown in Fig. 10b, together with the fit with Eq. (2). The down-curvature of the experimental data (and the fit) in the $T \to 0$ limit is due to the magnon contribution. The fit parameters are $\gamma = 10.2$ mJmol^{-1}K^{-2}, $\delta =$ 0.95 mJmol^{-1}K$^{-5/2}$ and $\theta_D = 406$ K (recall that this is the low-temperature θ_D value). The above γ value is close to the one of the Ce metal ($\gamma_{\mathrm{Ce}} = 12.8$ mJmol^{-1}K^{-2}), while the γ value of iron ($\gamma_{\mathrm{Fe}} = 4.9$ mJmol^{-1}K^{-2}) is considerably smaller (Si is a semiconductor).[22]

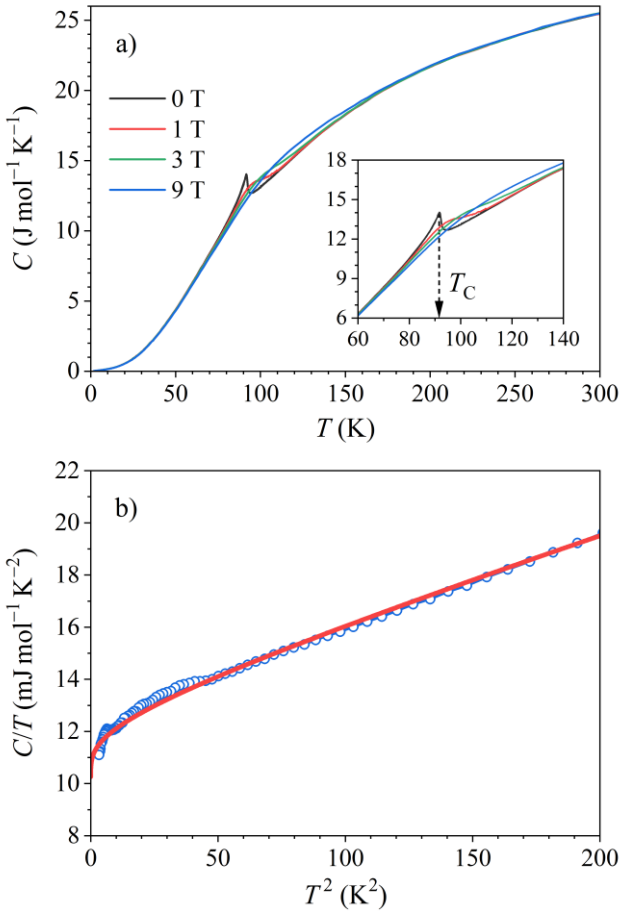

Fig. 10. (a) Total specific heat C of the $CeFe_9Si_4$ sample in the temperature range 2–300 K in selected magnetic fields between 0 and 9 T (values indicated on the graph). The inset shows the curves on an expanded scale within the phase-transition region. **(b)** Low-temperature zero-field specific heat in a C/T vs. T^2 plot. Red solid curve is the fit with Eq. (2) and the fit parameters are given in the text.

The magnetic specific heat C_m was extracted from the total specific heat C by treating the lattice contribution theoretically within the Debye model in the entire investigated temperature range using the formula[22]

$$C_D = 9Nk_B(T/\theta_D)^3 \int_0^{x_D} \frac{e^x x^4 dx}{(e^x-1)^2}. \quad (3)$$

Here N is the number of atoms in the crystal, $x = \hbar\omega/k_BT$, ω is the frequency of the lattice vibrations and $x_D = \theta_D/T$. It is known that for many solids the Debye model reproduces well

the experimental data at low temperatures $T < \theta_D/50$ (i.e. below about 2% of the Debye temperature, typically below 10 K) and at high temperatures $T > \theta_D/2$ (typically above 150–200 K). We have further assumed that $C_m = 0$ high in the paramagnetic phase (above 200 K, as estimated from the magnetoresistance) and very small in the $T \to 0$ limit. In the next step, we have calculated the specific heat $C_{calc} = \gamma T + C_D$ in the entire investigated temperature range 2–300 K, by adjusting the θ_D fit parameter while keeping the γ value determined before from the fit in Fig. 10b, to match C_{calc} to the experimental zero-field specific heat C in the high-temperature regime between 180 and 300 K. The theoretical C_{calc} obtained with the fit parameter value $\theta_D = 450$ K (the high-temperature θ_D value), together with the separated electronic (γT) and Debye (C_D) contributions is presented in Fig. 11a. The experimental total specific heat C in zero magnetic field and in a 9-T field is also shown, where excellent matching to C_{calc} in the interval 180–300 K is evident. The agreement of C_{calc} with C in the low-temperature limit $T \to 0$ is also good (C_{calc} and C are both very small there, so that any mismatch between them is not visible on the graph).

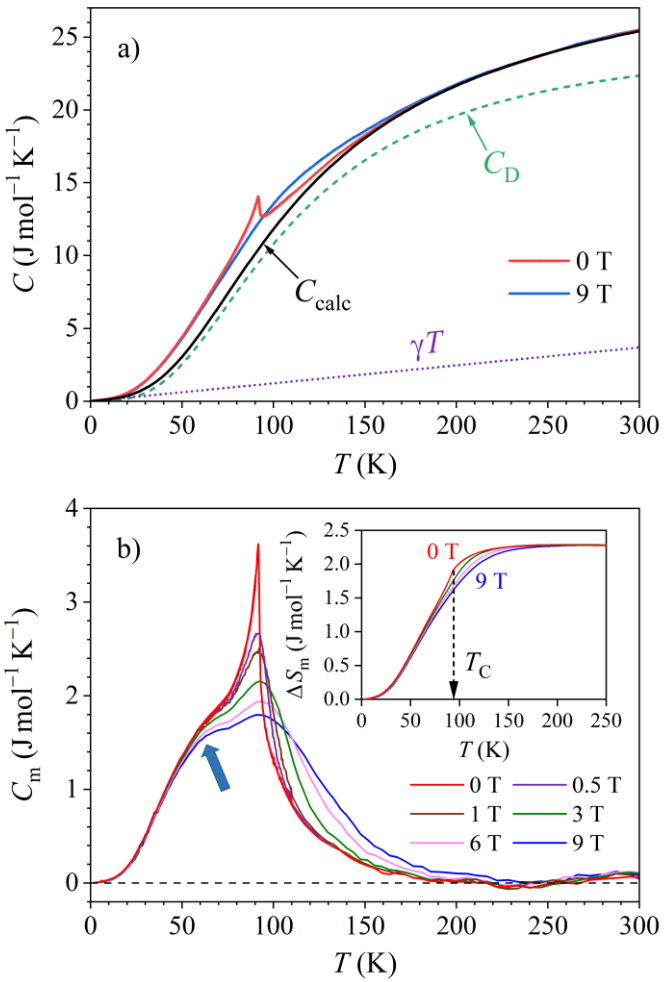

Fig. 11. (a) Experimental total specific heat C in zero- and 9-T magnetic fields, together with the calculated specific heat $C_{calc} = \gamma T + C_D$ in the temperature range 2–300 K. The electronic (γT) and Debye (C_D) contributions are also shown separately (details are described in the text). **(b)** Magnetic specific heat $C_m = C - \gamma T - C_D$ in different external magnetic fields (values indicated on the graph). The shoulder at about 60 K is indicated by an arrow. The inset shows the magnetic entropy $\Delta S_m(T) = S_m(T) - S_m(2K)$ in magnetic fields 0–9 T.

The magnetic specific heat was obtained by subtraction, $C_m = C - \gamma T - C_D$, and the procedure was repeated for the experimental specific heat measured in all magnetic fields. The graphs of $C_m(H,T)$ in the temperature range 2–300 K for all (seven) measured magnetic fields are shown in Fig. 11b. The zero-field magnetic specific heat $C_m(0,T)$ shows a sharp

peak at $T_C \approx 92$ K, which broadens and shifts to higher temperatures in an increasing magnetic field. This is the known smearing of the FM phase transition by the external magnetic field. The $C_m(H,T)$ curves show, however, an additional feature at lower temperatures deep inside the FM phase. The zero-field $C_m(0,T)$ exhibits a shoulder at about 60 K (marked by an arrow), which develops into a peak in an increasing field that largely overlaps with the main peak at 92 K (best seen on the 9-T curve). The origin of the shoulder will be discussed in the Discussion section. Here we note that this shoulder is in agreement with the shoulder observed in the temperature-dependent 6-T magnetoresistance presented in Fig. 9, occurring at practically the same temperature. We also emphasize that the Debye specific heat C_D and the electronic specific heat γT are both smooth functions of the temperature in the entire investigated temperature range, so that the shoulder in C_m could not be artificially created by the subtraction procedure, but is indeed a genuine property of the combined Ce–Fe spin system.

The magnetic entropy $\Delta S_m(T) = S_m(T) - S_m(2K) = \int_{2K}^{T} [C_m(T')/T']\, dT'$ in all magnetic fields is shown in the inset of Fig. 11b. As typical for the usual FM phases, most of the entropy lies above the ordering temperature T_C. The fact that the entropy does not reach the saturation plateau at $T_C \approx 94$ K, but still increases quite significantly up to about 150 K (in zero field) is a signal of magnetic short-range order in the paramagnetic phase. External magnetic field shifts the entropy to higher temperatures, as it locks the moments into the field direction and prevents their thermal disordering via spin fluctuations. The maximum (saturation) value of the entropy in the paramagnetic phase amounts to $S_m^{max} = 2.282$ $\mathrm{Jmol^{-1}K^{-1}}$ (by neglecting the vanishing small $S_m(2K)$), where this value applies to one mole of the $CeFe_9Si_4$ material. Recalculating per mole of the magnetic $CeFe_9$ "molecules", which is more appropriate for the discussion yields $S_m^{max} = 1.913$ $\mathrm{J(mol\text{-}CeFe_9)^{-1}K^{-1}}$.

5. DISCUSSION

Since the $CeFe_9Si_4$ contains the RE element Ce from the light half of the lanthanide series and the magnetic element Fe from the heavy half of the 3*d* series, ferromagnetism of this compound is not surprising. It can be predicted from the more general rule that exchange spin coupling between atoms possessing more than half full *d* shells with atoms possessing less than half full *d* shells is antiferromagnetic.[23] Due to the electronic configuration $4f^n5d^16s^2$, the RE atoms are in this context considered as light *d* elements. The coupling of spins of the ferromagnetic 3*d* transition elements TM = Fe, Co and Ni to the spins of the RE elements is therefore antiparallel. However, in light RE metals, the magnetic moment is mainly orbital in character and directed *opposite* to the spin according to Hund's third rule. Consequently, though the spins of the RE and TM atoms are antiparallel, their magnetic moments are parallel, resulting in ferromagnetism. Examples of the RE–TM ferromagnetic compounds that conform to this rule are the widely commercially used permanent magnets $SmCo_5$ and $Nd_2Fe_{14}B$ (and their derivatives), in which the RE moments are localized, while the 3*d* moments are itinerant.[24]

The FM transition temperature $T_C \approx 94$ K of the $CeFe_9Si_4$ is considerably higher than the T_Cs of isotypic ferromagnetic RE-containing compounds without a magnetic 3*d* transition element. Examples are the $RECu_9Sn_4$ (RE = Ce, Pr, Nd and Eu) compounds with T_Cs of 5.5, 10.5, 15 and 10.5 K, respectively.[11–13] The magnetism of these compounds originates solely from the RE atoms and the relatively low T_Cs are considered to be related to the large nearest-neighbor RE–RE distances of about 6 Å, which make the indirect exchange (Ruderman-Kittel-Kasuya-Yosida – RKKY) interaction between the localized RE moments weak. In the

$CeFe_9Si_4$, there are two sources of magnetism, the localized Ce^{3+} $4f$ moments and the itinerant Fe $3d$ moments. The Ce–Ce nearest-neighbor distances of about 5.6 Å are also large, so that the RKKY interaction between the Ce moments cannot account for the strong increase of T_C. Instead, the higher T_C of $CeFe_9Si_4$ is the effect of iron. The type of exchange interaction between the localized Ce and the delocalized Fe moments (either direct exchange or RKKY indirect exchange) is a subtle question, because it depends on the degree of the Fe moments delocalization. However, since the Ce distances to the Fe1 and Fe2 atoms that constitute the 24-atom cage around the Ce atom are considerably shorter (Ce–Fe1 3.24 Å, Ce–Fe2 3.35 Å), the Ce–Fe exchange interactions must be stronger, shifting the T_C of $CeFe_9Si_4$ to higher temperatures. A quantitative theoretical treatment of magnetism of the combined Ce–Fe system with localized Ce moments and delocalized Fe moments in the presence of three kinds of exchange interactions (Ce–Ce, Ce–Fe and Fe–Fe) is very complex and remains a challenge for future studies.

The fact that the small, temperature-independent hysteresis in the $M(H)$ curves of the $CeFe_9Si_4$ sample was experimentally observed also at 400 K (high above the FM transition temperature $T_C \approx 94$ K) strongly suggests that the observed hysteresis originates from the Fe_3Si impurity phase, while the $CeFe_9Si_4$ phase possesses vanishing small magnetic anisotropy and is hence magnetically soft. The reason for the vanishing anisotropy is not obvious. The magnetocrystalline anisotropy is straightforward to discuss for the RE ions, which possess well-localized $4f$ magnetic electrons. The electric charge $e\rho_{4f}(\vec{r})$ of the Ce^{3+} $4f$ shell is not spherically symmetric, but oblate (flattened). It is coupled to the electrostatic potential $\varphi_{cf}(\vec{r})$ of the surrounding crystal charges, resulting in the crystal-field anisotropy energy $\varepsilon_a = \int e\rho_{4f}(\vec{r})\varphi_{cf}(\vec{r})\, d^3r$. Expanding the $4f$ charge density in spherical harmonics, the leading term in ε_a is the coupling of the ρ_{4f} quadrupole moment Q_2 (which is negative

for the Ce^{3+} oblate ion) to the electric field gradient (EFG) tensor created by the crystal charge distribution at the cerium site. For the tetragonal symmetry of the unit cell, the EFG tensor V_{ij} in the crystal-fixed reference frame (a,b,c) is diagonal, having the eigenvalues $V_{aa} = V_{bb} = -V/2$ and $V_{cc} = V$. This makes the c crystallographic direction (the tetragonal axis) the easy direction of magnetization, with anisotropy to the (a,b) tetragonal plane. At low temperatures, higher moments (hexadecapole and 64-pole moments, Q_4 and Q_6) of the 4f charge density become also important and the anisotropy energy for the tetragonal symmetry depends both on the polar angle θ between the magnetization and the tetragonal (easy) direction and the azimuthal angle ϕ in the tetragonal plane. There is, therefore, no *a priori* reason for the vanishing magnetocrystalline anisotropy based on symmetry considerations of the tetragonal unit cell. Strong magnetocrystalline anisotropy of the RE magnetization, with the easy axis along [001] and hysteretic $M(H)$ curve was indeed observed experimentally in the $RECu_9Sn_4$ (RE = Ce, Pr) compounds,[12] suggesting that the Ce fraction of magnetization in the $CeFe_9Si_4$ should also be anisotropic and introduce some hysteresis in the total magnetization (Ce + Fe) of this phase, in contrast to the experimental finding that the phase is magnetically soft. The Fe itinerant magnetism in the $CeFe_9Si_4$ phase is obviously soft, while there can be various reasons why the anisotropic magnetism of the Ce subsystem has not been observed experimentally in the total magnetization. One possibility is a significant reduction of the Ce magnetic moment by the crystal fields, which would happen when the ground state doublet of the three crystal-field-split doublets of the Ce^{3+} $J = 5/2$ states would be populated only, the other two being too high in energy. The second possibility follows from the analogy to the strongly anisotropic magnetism in the related $CeCu_9Sn_4$ single crystal.[12] There, the Ce magnetization within the FM phase for the field along the [001] easy axis saturates at 0.1 T and the saturated moment reaches 1.75μ_B (slightly reduced with

respect to the Ce^{3+} free-ion saturated value of $2.14\mu_B$, very likely due to the crystal fields), while the magnetization for the field along the [100] perpendicular direction is almost negligibly small (verified up to 1 T). For a polygrain material with randomly oriented microcrystallites (like our investigated $CeFe_9Si_4$ sample), such anisotropic magnetization can average to a quite small value and becomes experimentally unobservable in the presence of another (larger) source of magnetization, like the magnetically soft Fe magnetization.

The analysis of the magnetic entropy can be performed based on the maximum entropy of the paramagnetic phase that amounts to $S_m^{max} = 1.913$ J(mol-$CeFe_9$)$^{-1}$K^{-1}. Adopting the approximation that this entropy can be written as a sum $0.1S_m^{Ce} + 0.9S_m^{Fe}$, where S_m^{Ce} and S_m^{Fe} are the molar magnetic entropies of the Ce and Fe subsystems, respectively, we write for the localized Ce magnetic moments $0.1S_m^{Ce} = 0.1Rln(2J+1)$. If only the lowest crystal-field-split doublet would be populated ($J = 1/2$), this yields $0.1S_m^{Ce} = 0.58$ Jmol^{-1}K^{-1}, while for all three doublets of $J = 5/2$ populated, the value is 1.49 Jmol^{-1}K^{-1}. Both values are smaller than the experimental S_m^{max}, so that the rest of the magnetic entropy must come from the Fe subsystem. Since there is no clear way on how to separate the contributions of the Ce (localized) and Fe (itinerant) subsystems of magnetic moments to the total magnetic entropy, the analysis of the crystal-field splitting of the Ce magnetic levels is inconclusive.

We discuss next the possible origin of the shoulder that appears in the magnetic specific heat and in the temperature-dependent magnetoresistance curve inside the FM phase much below the main peak at T_C. In the case of the magnetic specific heat, the shoulder reflects an increasing FM spin order in the combined Ce–Fe spin system upon cooling below T_C, which is manifested as an increased heat release from the system due to lowering of the magnetic energy. It is well known that the FM-ordered moments in a crystal may distort the lattice and change the lattice parameters via the magnetoelastic coupling. This is the

phenomenon of volume magnetostriction,[25] a temperature-dependent effect that is proportional to the square of the spontaneous magnetization, $M(T)^2$. The changed lattice parameters reflect the modified distances between the atoms in the unit cell, which in turn change the electronic band structure, the exchange coupling, the magnetic dipole interactions and the crystal fields. Ferromagnetic ordering may thus have a profound effect on the electronic, magnetic, thermal and optical properties of a solid. In the $CeFe_9Si_4$ compound, it is plausible to consider that the growing magnetization of the Ce–Fe system below T_C imposes a temperature-dependent change of the electronic band structure that alters the band magnetism of the itinerant Fe moments in a way to further increase the FM ordering. This produces a shoulder in the magnetic specific heat deep inside the FM phase. The increased FM order similarly affects the magnetotransport, because larger magnetization increases the (absolute) magnetoresistance. Since the temperature evolution of the shoulder in the magnetoresistance curve of Fig. 9 is very much the same as that of the shoulder in the magnetic specific heat in Fig. 11b, the two shoulders obviously share common origin, considered to be the magnetization-induced change of the electronic band structure that alters the Fe band magnetism. The above considerations offer a plausible hypothesis, which still needs to be proven by the electronic band structure calculations for the $CeFe_9Si_4$ structure in the presence of magnetoelastic effects. Such demanding *ab initio* calculations go beyond the scope of this paper.

Finally, we comment on the influence of the Fe_3Si and $CeFe_2Si_2$ impurity phases in the investigated $CeFe_9Si_4$ material on the analysis and properties of the $CeFe_9Si_4$ ferromagnetic phase. The content of the $CeFe_2Si_2$ Pauli-paramagnetic impurity phase (about 0.5 wt.%) is so low that it cannot significantly influence the magnetism of the $CeFe_9Si_4$ phase and can hence be neglected. The Fe_3Si phase is present in more significant amount (5.7 wt.%)

and its ferromagnetism with $T_C \approx$ 840 K was indeed experimentally observed in the temperature-dependent magnetization and the $M(H)$ curves of the investigated $CeFe_9Si_4$ material, but due to the very high value of the T_C, the magnetization M_{FS} is practically constant in the temperature range of the FM phase in the $CeFe_9Si_4$ (below $T_C \approx$ 94 K) and could be reliably subtracted from the total $M(T)$ magnetization, to yield the magnetization M_{CFS} of the $CeFe_9Si_4$ phase only. Proper identification of the M_{FS} could also be done in the $M(H)$ curves. For the magnetoresistance, the presence of the two impurity phases is unimportant, because the precipitates are well isolated in space from each other and do not yield a connected path in the material from one to the other electrode to allow current flow via the impurity phases. The specific heat within the experimentally studied temperature range below 300 K is also practically insensitive to the presence of the impurity phases, due to their low amount and the high Curie temperature of the Fe_3Si phase. The performed analysis of ferromagnetism in the $CeFe_9Si_4$ phase should hence be correct.

6. CONCLUSIONS

We have determined the crystal structure of the $CeFe_9Si_4$ intermetallic compound and found that the revised structural model agrees with the previous one,[3] with some minute quantitative differences. Cerium atoms are located in the centers of highly symmetric cages, the 24-atom polyhedra composed of the Fe1, Fe2 and Si atoms, while the Fe3 atoms are located in the centers of icosahedra composed of the Fe1, Fe2 and Si atoms that already belong to the 24-atom cages. This type of structure is not unique to the $CeFe_9Si_4$ compound, but was found before in the ACu_9X_4 (A = Sr, Ba; X = Si, Ge) series, $LaFe_9Si_4$, $CeNi_9Si_4$ and $RECu_9Sn_4$ (RE = La, Ce, Pr, Nd, Eu and Yb).

The measurements of magnetization, magnetoresistance and magnetic specific heat have revealed that $CeFe_9Si_4$ undergoes a ferromagnetic transition at the Curie temperature $T_C \approx$ 94 K. Ferromagnetism in the combined Ce–Fe spin system is a result of interplay between the localized magnetism on the Ce sublattice and the Fe band (itinerant) magnetism. It follows from the general rule that the exchange spin coupling between atoms possessing more than half full *d* shells with atoms possessing less than half full *d* shells is antiferromagnetic (where the Ce atoms are considered as light *d* elements). Since in light RE metals, the magnetic moment is directed opposite to the spin, this results in ferromagnetism. The magnetoresistance and the magnetic specific heat show additional temperature-dependent feature (a shoulder) deep inside the ferromagnetic phase that is considered to originate from the influence of the magnetization on the electronic band structure via the magnetoelastic coupling, which alters the Fe band magnetism below T_C in a temperature-dependent manner. This hypothesis still needs to be proven by the electronic band structure calculations in the presence of magnetoelastic effects. The FM phase of the $CeFe_9Si_4$ is magnetically soft. Unlike the isostructural $CeNi_9Si_4$ compound, which shows Kondo lattice behavior and Ni is in a nonmagnetic state, Fe is magnetic in the $CeFe_9Si_4$ compound, leading to ferromagnetism of the combined Ce–Fe spin system.

7. EXPERIMENTAL SECTION

Powder XRD was performed using a Bruker D8 Advance diffractometer in Bragg-Brentano $\theta/2\theta$ configuration. The wavelength was a Johansson Ge(111) monochromated Cu Kα_1 ($\lambda = 1.54056$ Å). The sample was finely ground in an agate mortar and deposited in zero-background sample holder. The data were collected with a 0.021^{o} step 2θ width and 4 sec

counting time per point over the 2θ range from 10^{o} to 130^{o}. The sample was allowed to rotate perpendicular to the diffusion plane at a speed of 15 rev/min. The detection was performed using a LynxEye PSD detector in 1D. The analysis of the diffraction patterns was performed by Rietveld profile refinement using the FullProf and WinPlotr software packages.[4,26,27]

Single-crystal XRD data were collected on a Bruker Kappa Apex II diffractometer equipped with a mirror monochromator and a Mo Kα microsource ($\lambda = 0.71073$ Å). The Apex2 program package was used for the cell refinement and data reduction. The structure was solved by using direct methods and refined with the SHELXL-2014 program package.[28] Semi-empirical absorption correction (SADABS) was applied to the data.

SEM BSE imaging and EDS chemical composition determination were performed by a scanning electron microscope ThermoFisher Quanta 650 ESEM equipped with EDS Oxford Instruments, AZtecLive, Ultim Max SDD 40 mm^2.

HAADF-STEM imaging was performed by a JEM-ARM 200F Cold FEG TEM/STEM transmission electron microscope operating at 200 kV, coupled with a GIF Quantum 965 ER and equipped with a spherical aberration (Cs) probe and image correctors (point resolution 0.12 nm in the TEM mode and 0.078 nm in the STEM mode). Atomically resolved STEM images were processed using an Average Background Subtraction Filter (ABSF)[29] to increase the signal-to-background ratio. The collection semi-angle for the HAADF-STEM detector was set between 68 and 280 mrad. For the TEM specimen preparation, a $CeFe_9Si_4$ sample was cut into blocks and mounted face-to-face in a brass ring of 3 mm in diameter with epoxy glue. The mounted sample was then mechanically ground to a thickness of 100 μm and dimpled down to 15 μm at the disc center (Dimple grinder, Gatan Inc., Warrendale, PA). The TEM specimen was finally ion-milled (PIPS, Precision Ion

Polishing System, Gatan Inc., Warrendale, PA) using 3 kV Ar^+ ions at an incidence angle of 8^o until perforation.

Magnetization measurements were conducted on a Quantum Design MPMS3 SQUID magnetometer equipped with a 7 T magnet, operating in the temperature range 2–1000 K.

Electrical resistivity, magnetoresistance and specific heat were measured on a Quantum Design Physical Property Measurement System (PPMS 9T) equipped with a 9 T magnet and operating in the temperature range 2–400 K.

Acknowledgments

The Slovenian authors acknowledge financial support from the Slovenian Research Agency (research core funding No. P1-0125 and P2-0084). This work is a result of a cooperation within the French-Slovene collaboration established under the International Research Project (IRP) Push-Pull Alloys and Complex Compounds ($PACS_2$). The INC CNRS and the Université de Lorraine are acknowledged for financially supporting the IRP $PACS_2$.

Author Contributions

The manuscript was written through contributions of all authors. All authors have given approval to the final version of the manuscript.

Notes

The authors declare no competing financial interest.

References

(1) Sereni, J. *Handbook on the Physics and Chemistry of Rare Earths*; Gschneidner, K. A. Jr., Eyring, L., Eds.; North-Holland: Amsterdam, The Netherlands, 1991; Vol. 15, pp 1–59.

(2) Michor, H.; Berger, St.; El-Hagary, M.; Paul, C.; Bauer, E.; Hilscher, G. Crystal structure and Kondo lattice behavior of $CeNi_9Si_4$. *Phys. Rev. B* **2003**, *67*, 224428.

(3) Berthebaud, D.; Tougait, O.; Potel, M.; Noël, H. Isothermal section at 900 ^{o}C of the Ce–Fe–Si ternary system. *J. Alloys Compd*. **2007**, *442*, 104–107.

(4) Rodríguez-Carvajal, J. Fullprof: A program for Rietveld refinement and pattern matching analysis; *Abstract of the Satellite Meeting on Powder Diffraction of the XV Congress of the IUCr*: Toulouse, France, 1990; p. 127.

(5) Lin, M.-C.; Barnes, R. G.; Torgeson, D. R. Mössbauer-effect study of ferromagnetic $D0_3$-structured iron-aluminum-silicon alloys. *Phys. Rev. B* **1981**, *24*, 3712–3718.

(6) Niculescu, V. A.; Burch, T. J.; Budnick, J. I. A local environment description of hyperfine fields and atomic moments in $Fe_{3-x}T_xSi$ alloys. *J. Magn. Magn. Mater.* **1983**, *39*, 223–267.

(7) Ammarguellat, C.; Escorne, M.; Mauger, A.; Beaurepaire, E.; Ravet, M. F.; Krill, G.; Lapierre, F.; Haen, P.; Godart, C. Mixed valence properties of CeM_2Si_2 (M = Mn, Fe, Co, Ni, Cu). *Phys. Stat. Sol. (b)* **1987**, *143*, 159–166.

(8) Mihalik, M.; Mihalik, M.; Sechovský, V. Electrical transport and magnetism in $CeFe_2Si_2$ single crystal. *Physica B* **2005**, *359–361*, 163–165.

(9) Kranenberg, C.; Mewis, A. ACu_9X_4 – New compounds with $CeNi_{8,5}Si_{4,5}$ structure (*A*: Sr, Ba; *X*: Si, Ge). *Z. Anorg. Allg. Chem*. **2003**, *629*, 1023–1026.

(10) Tang, W.-H.; Liang, J.-K.; Chen, X.-L.; Rao, G.-H.; Structure of $LaFe_9Si_4$ intermetallic compound. *J. Appl. Phys*. **1994**, *76*, 4095–4098.

(11) Singh, S.; Fornasini, M. L.; Manfrinetti, P.; Palenzona, A.; Dhar, S. K.; Paulose, P. L. Crystallographic and magnetic behaviour of RCu_9Sn_4 and $RCu_{9.4}Sn_{3.6}$ (R = La to Nd) compounds. *J. Alloys Compd.* **2001**, *317–318*, 560–566.

(12) Hirose, Y.; Tomaru, S.; Satoh, S.; Ota, S.; Kurahashi, S.; Takeuchi, T.; Honda, F.; Homma, Y.; Li, D.; Aoki, D.; Settai, R. *J. Phys. Conf. Ser.* **2015**, *592*, 012034.

(13) Mazzone, D.; Paulose, P. L.; Dhar, S. K.; Fornasini, M. L.; Manfrinetti, P. Crystal structure and magnetic properties of ordered phases in the Eu–Cu–Sn system. *J. Alloys Compd.* **2008**, *453*, 24–31.

(14) Fornasini, M. L.; Manfrinetti, P.; Mazzone, D.; Riani, P.; Zannichi, G. Crystal structure of ytterbium copper stannides in the range 14–32 at.% tin. *Intermetallics* **2006**, *14*, 272–279.

(15) Jensen, J.; Mackintosh, A. R. *Rare Earth Magnetism*; Clarendon Press: Oxford, UK, 1991; p 57.

(16) See, e.g., Ashcroft, N. W.; Mermin, N. D. *Solid State Physics*; Saunders College: Philadelphia, PA, 1976; pp 644–658.

(17) Kasuya, T. Electrical resistance of ferromagnetic metals. *Prog. Theor. Phys*. **1956**, *16*, 58–63.

(18) Fisher, M. E.; Langer, J. S. Resistive anomalies at magnetic critical points. *Phys. Rev. Lett*. **1968**, *20*, 665–668.

(19) Kudrnovský, J.; Drchal, V.; Turek, I.; Khmelevskyi, S.; Glasbrenner, J. K.; Belashchenko, K. D. Spin-disorder resistivity of ferromagnetic metals from first principles: The disordered-local-moment approach. *Phys. Rev. B* **2012**, *86*, 144423.

(20) Yamada, H.; Takada, S. Magnetoresistance of antiferromagnetic metals due to *s-d* interaction. *J. Phys. Soc. Jpn*. **1973**, *34*, 51–57.

(21) Yamada, H.; Takada, S. Negative magnetoresistance of ferromagnetic metals due to spin fluctuations. *Prog. Theor. Phys*. **1972**, *48*, 1828–1848.

(22) Tari, A. *The Specific Heat of Matter at Low Temperatures*; Imperial College Press: London, UK, 2003; pp 26–35 and 69–71 and 148–153.

(23) Coey, J. M. D. *Magnetism and Magnetic Materials*; Cambridge University Press: Cambridge, UK, 2010; p 154.

(24) Wallace, W. E. *Rare Earth Intermetallics*; Academic Press: New York, NY, 1973; Chs. 10 and 11.

(25) Shiga, M. Magnetovolume effects of Fe alloys: Magnetic moment as a function of atom distance. *IEEE Transl. J. Magn. Jpn.* **1991**, *6*, 1039–1049.

(26) Rodríguez-Carvajal, J. Recent advances in magnetic structure determination by neutron powder diffraction. *Physica B Condens. Matter* **1993**, *192*, 55–69.

(27) Roisnel, T.; Rodríguez-Carvajal, J. WinPLOTR: A Windows tool for powder diffraction pattern analysis. *Mater. Sci. Forum* **2001**, *378–381*, 118–123.

(28) Sheldrick, G. M. Crystal structure refinement with SHELXL. *Acta Cryst. C* **2015**, *71*, 3–8.

(29) Kilaas, R. Optimal and near-optimal filters in high-resolution electron microscopy. *J. Microsc.* **1998**, *190*, 45–51.

For Table of Contents only

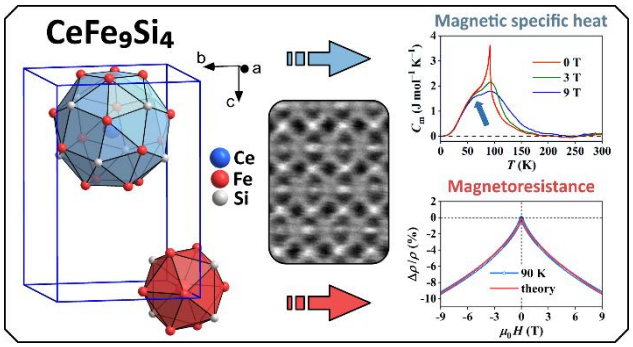

Synopsis

In a search for cerium-containing intermetallic compounds with uncommon magnetic and electrical transport properties, we have synthesized the $CeFe_9Si_4$ compound and determined its crystal structure and magnetic properties. Based on the measurements of magnetization, magnetoresistance and magnetic specific heat, the compound is a soft ferromagnet below $T_C = 94$ K.